applied optics

# Optical constants of TiN, amorphous $SiO_2$, and SiN in the extreme ultraviolet range

Qais Saadeh,[1,*] Vicky Philipsen,[2] Johan Meersschaut,[2] Venkat Sunil Kumar Channam,[2] Karim-Alexandros Kantre,[2] Andrey Sokolov,[3] Bettina Kupper,[1] Thomas Wiesner,[1] Danilo Ocaña García,[1] Zanyar Salami,[1] Christian Buchholz,[1] Frank Scholze,[1] and Victor Soltwisch[1]

[1]Physikalisch-Technische Bundesanstalt (PTB), Abbestraße 2-12, 10587 Berlin, Germany
[2]imec, Kapeldreef 75, B-3001 Leuven, Belgium
[3]Helmholtz-Zentrum Berlin für Materialien und Energie, Elektronenspeicherring BESSY II, 12489 Berlin, Germany
*qais.saadeh@ptb.de

Received 23 September 2024; revised 18 November 2024; accepted 19 November 2024; posted 20 November 2024; published 9 December 2024

**Using reflectometry, we studied the optical constants of TiN and amorphous $SiO_2$ thin films in the spectral range 5–24 nm (ca. 250 eV–ca. 52 eV), and for SiN in the spectral range 5–33 nm (ca. 250 eV–ca. 37 eV). The films' elemental concentration depth profiles were measured using elastic recoil detection analysis (ERDA). The reflectance was measured using monochromatized synchrotron radiation. For the analysis of reflectivity data, Markov chain Monte-Carlo (MCMC)-based Bayesian inferences Bayesian inferences were used to obtain the optical constants and their model uncertainties. For $SiO_2$ and SiN, dispersion profiles were sampled with sub-Ångström resolution in certain intervals around the Si-$L_1$ and Si-$L_{2,3}$ transitions. The obtained optical constants are compared with literature values and with estimations based on the independent atom approximation (IAA).**

Published by Optica Publishing Group under the terms of the Creative Commons Attribution 4.0 License. Further distribution of this work must maintain attribution to the author(s) and the published article's title, journal citation, and DOI.

https://doi.org/10.1364/AO.542950

## 1. INTRODUCTION

The sub-extreme ultraviolet (EUV) spectral range between 5 and 33 nm (ca. 250 eV to ca. 37 eV) is critical for many applications, microscopy [1], ptychography [2], spectrometry [3], astronomy [4], and most notably lithography. ASML's first commercial high-numerical-aperture (high-NA) extreme ultraviolet lithography (EUVL) systems are planned for deployment in 2025, enabling 8-nm resolution [5]. While using a wavelength of 13.5 nm, EUVL systems can be even further tweaked to print with higher resolution [6], unlocking future scopes for the integrated circuit (IC) industry. However, all those applications and their undergoing developments rely on improving the optical elements. For that, the optical constants are essential since materials screening and selection processes mainly regard the optical and chemical properties [7]. A manifestation for the importance of accurate optical constants is their need in developing photomasks for future EUVL projection systems [8].

In the X-ray and EUV spectral ranges, the optical constants are often denoted as $\delta$ and $\beta$. These are the two parts of the complex index of refraction $\bar{n}$, which is given as a function of the wavelength $\lambda$ as $\bar{n}(\lambda) = 1 - \delta(\lambda) + i\beta(\lambda)$. For a defined medium given a specific wavelength, the real part $(1 - \delta)$ is called the refractive index (or the index of refraction) and counts for the phase velocity. The imaginary part $\beta$ is called the extinction coefficient and counts for absorption. Despite their importance, the available optical data for compounds in the X-ray and EUV spectral ranges has limitations. Inconsistencies between different sources, improper sampling of dispersion profiles, and lack of calculated uncertainties are often observed in the available optical data for compounds. Another common critical issue is the lack of information about the real stoichiometry of the investigated compounds. These issues encourage examining the optical constants of technologically relevant materials.

In our work, we report the determination of TiN and amorphous $SiO_2$ optical constants in the spectral range 5–24 nm (ca. 250 eV–ca. 52 eV), and for SiN in the spectral range 5–33 nm (ca. 250 eV–ca. 37 eV). The optical constants were determined using synchrotron reflectometry. The three compounds have been extensively investigated before and found applications in the X-ray and EUV spectral ranges. A plus for these compounds is that their constituents are highly abundant [9]. Starting with TiN films, they are known for their high chemical stability and mechanical durability [10]. TiN thin films were used in X-ray reflectometry (XRR) for demonstrations [11,12], presumably, due to their known traits. TiN thin films deposited

using radio frequency physical vapor deposition (RFPVD) were found suitable for EUVL patterning applications given their uniformity and relatively small grains [13]. TiN was investigated as a capping layer for Mo/Si multilayer mirrors (MLMs) dedicated for EUVL systems [14], also as a constituent of photomasks' absorbers [15]. Yeo *et al*. showed a TiN thin film resisting etching against harsh hydrogen plasma for up to 3 min, demonstrating the material's potential for capping EUVL pellicles [16]. Braic *et al*. presented ZrN/TiN MLMs intended for EUVL [17].

Among Si-N materials, which refer to the compounds covered by the stoichiometry $SiN_x$ with $0 < x < 1.33$ [18], $Si_3N_4$ is probably the most ubiquitous in EUV optics. $Si_3N_4$ is chemically stable with a high melting point (ca. 2700 K) and has a transient optical response in the EUV range [19]. These properties made it popular for femtosecond time-diagnostics in free-electron laser (FEL) light sources at EUV wavelengths [19,20]. $Si_3N_4$ has also been investigated and used due to its relatively low absorptance in the soft X-ray and EUV spectral ranges [21]. In the Physikalisch-Technische Bundesanstalt (PTB), the EUV transmittance of $Si_3N_4$ windows and filters was measured before [22,23]. Solak *et al*. used a membrane window made of $Si_3N_4$ to keep the vacuum environment of their EUV beamline [24]. Jimenez *et al*. studied the transmittance of Nb-Zr thin film filters on $Si_3N_4$ membranes in the spectral range 3–31 nm [25]. Cho *et al*. investigated the transmittance of EUV pellicles made of silicon nitride [26]. Rothhardt *et al*. used $Si_3N_4$ membranes for preparing germlings intended for EUV microscopy at a wavelength of 13.5 nm [27]. Aminzadeh *et al*. reported fabricating $Si_3N_4$ diffractive optics for the soft X-ray and EUV spectral ranges [21]. Bruijn *et al*. used $Si_3N_4$ as an interdiffusion barrier for Mo-on-Si interfaces [28], which can be relevant when investigating the development of EUV multilayer mirrors (MLMs). Boher *et al*. reported the relatively high thermal stability of Si/$Si_3N_4$ MLMs designed for the soft X-ray and EUV spectral ranges [29].

For the third material in our study, $SiO_2$, the fact that it can easily grow on Si substrates gave the latter an advantage over other substrates such as Ge, given $SiO_2$ high stability [30]. The nanoscale properties of $SiO_2$−Si interfaces are well-understood [31], and the very thin $SiO_2$ layers that naturally passivate Si substrates are usually amorphous [32]. Therefore, accurate optical data for amorphous $SiO_2$ can help in improving modeling the optical responses of Si-based optical elements and photodiodes. Amorphous $SiO_2$ films emission and absorption spectra in the EUV were studied before [33,34]; therefore, additional studies on the material can help for better understanding and verification. Also, $SiO_2$ films have been used as buffer layers to protect EUVL MLMs during absorber repairs [35]. Wang *et al*. reported Mo/$SiO_2$ intended for the spectral range 2.0–4.5 nm, emphasizing that $SiO_2$ can be considered "good" as a MLM spacer material in that range [36].

The optical constants of SiN, quartz and amorphous $SiO_2$ were investigated before in the EUV range [37–43]. However, in comparison against our results, differences were found. As well, we examine the accuracy of the independent atom approximation (IAA) for estimating the optical constants of TiN, SiN, and amorphous $SiO_2$ [44].

## 2. EXPERIMENTAL METHODS

### A. Samples Fabrication and Stoichiometry Profiling

The thin films were deposited on semiconductor-grade polished Si substrates. SiN and $SiO_2$ thin films were grown using plasma-enhanced chemical vapor deposition (PECVD). Both SiN and $SiO_2$ thin films had nominal thicknesses of 50 nm. Also, a TiN thin film with a nominal thickness of 30 nm was grown by physical vapor deposition (PVD).

The elemental concentration depth profiles were obtained from time-of-flight energy elastic recoil detection analysis (ToF-E ERDA) [45]. A primary beam of 8.028 MeV $^{35}Cl^{4+}$, sample tilt of 15°, and a scattering angle of 40° was used. The elemental depth profiles are shown in Fig. 1. From the depth profiles, the compositions below the surface are determined as follows: $SiO_2 = Si_{0.29}O_{0.63}H_{0.056}$; $SiN = Si_{0.331}N_{0.404}H_{0.262}$ and $TiN = Ti_{0.47}N_{0.52}$. In the depth profiles a limited amount of oxygen is noticed at the surface interface for the SiN and TiN layers. A significant amount of hydrogen is detected for SiN.

### B. Reflectivity Measurement Settings

For TiN and $SiO_2$, the specular reflectance was measured in the soft X-ray radiometry laboratory of the PTB (SX700 beamline), at the third generation electron storage ring BESSY II. The beamline and reflectometer with which the data was collected are described in detail in Refs. [46–48].

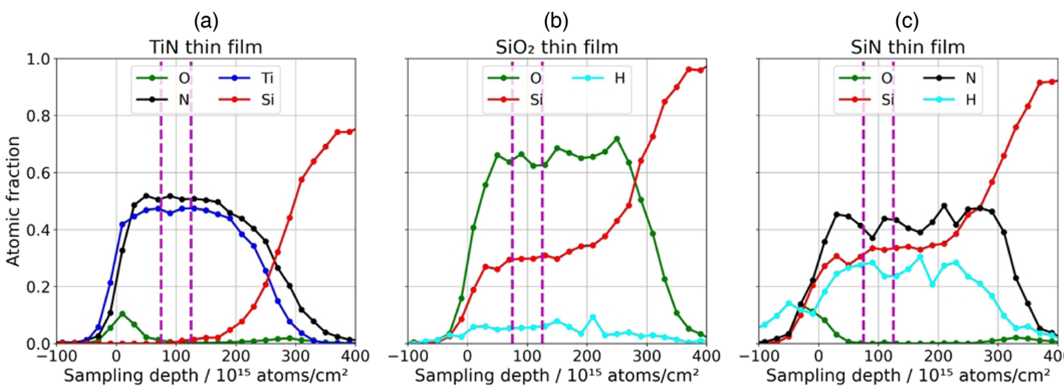


**Fig. 1.** ERDA profiles from twin samples of the thin films studied here. The dashed-vertical lines mark the sampling depths from which the stoichiometries are calculated. (a) Profiles from the TiN coating. (b) Profiles from the $SiO_2$ coating. (c) Profiles from the SiN coating.

**Table 1. Settings at Which the Presented Reflectance Data Were Collected from the TiN and $SiO_2$ Samples at the SX700 Beamline[a]**

| TiN | | Amorphous $SiO_2$ | |
|---|---|---|---|
| λ-Range (step)/nm | Angular Range (step)/° | λ-Range (step)/nm | Angular Range (step)/° |
| 4.5–8.0 (0.25) | 5.0–51.0 (0.5) | 5.0–6.0 (0.25) | 4.0–80.0 (1.0) |
| | | 6.1–7.6 (0.1) | 4.0–80.0 (1.0) |
| | | 7.7–7.99 (0.01) | 5.0–51.0 (1.0) |
| 8.5–24 (0.25) | 5.0–80.0 (1.5) | 8.0–10.4 (0.1) | 4.0–80.0 (1.0) |
| | | 10.5–12.1 (0.01) | 5.0–51.0 (1.0) |
| | | 12.2–15.0 (0.1) | 4.0–80.0 (1.0) |
| | | 15.5–24.5 (0.5) | 4.0–80.0 (1.0) |

[a]The values in brackets denote the step size.

**Table 2. Settings at Which the Presented Reflectance Data Were Collected at the Optics Beamline from the SiN Sample[a]**

| λ-Range (step)/nm | Angular Range (step)/° |
|---|---|
| 5.0–7.0 (0.2) | 2.5–35.0 (0.5) |
| 7.1–8.15 (0.01) | 3.0–50.0 (1.0) |
| 8.2–9.9 (0.1) | 2.5–40.0 (0.5) |
| 10.0–11.0 (0.1) | 3.0–65.0 (1.0) |
| 11.1–11.5 (0.01) | 3.0–50.0 (1.0) |
| ca. 11.53–ca. 12.27 (variable steps) | 2.0–45.0 (1.0) |
| 12.4–12.9 (0.1) | 3.0–65.0 (1.0) |
| 13.0–16.0 (0.5) | 3.0–65.0 (1.0) |
| 16.5–25.0 (0.5) | 4.0–80.0 (2.0) |
| 26.0–33.0 (1.0) | 6.0–80.0 (2.0) |

[a]The values in brackets denote the step size.

The presented reflectance data for the TiN and $SiO_2$ samples are made up of 78 scans and 285 scans, respectively. The scans were measured in the spectral range 4.5–24.5 nm with the settings given in Table 1. The angles given in Table 1 regard the grazing incidence geometry.

For the amorphous $SiO_2$ coating, two coupons diced from the same 300 mm wafer were measured. One coupon (C-$SiO_2$ -A) measured in the spectral ranges 5.0–7.5 nm, 8.1–10.4 nm, and 12.2–24.5 nm, and another coupon measured in the rest (at absorption edges, denoted here as C-$SiO_2$ -B). The coupons' designations will be used in the remaining sections.

The reflectivity data was measured using S-polarized radiation. Fine steps were used for measuring the $SiO_2$ sample, particularly for the spectral ranges 7.7–8 nm and 10.5–12.1 nm (Table 1). Those steps were implemented to account for the fine-structure due to the known Si-$L_1$ and Si-$L_{2,3}$ transitions [49].

For SiN, a coupon with approximate dimensions of 20 mm × 45 mm was measured at the Optics Beamline of Helmholtz-Zentrum Berlin für Materialien und Energie (HZB), also in the storage ring BESSY II [50]. 270 scans are presented in our report from the SiN sample; the settings are listed in Table 2.

The variable settings for measuring the reflectance of the SiN sample were implemented for the proper sampling of the observed fine-structure. In comparison with $SiO_2$, a more intricate fine-structure is observed.

## 3. SAMPLES REFLECTIVITY MODELING

Determining optical constants using reflectometry is based on the convergence of an inverse-problem. In such a problem, an assumed model for a sample is given with the corresponding expectation ranges for its optical and structural characteristics. Those expectation ranges resemble our best prior knowledge about the targeted parameters. We set the expectation ranges for the optical constants here around the Center for X-Ray Optics (CXRO) tabulations [44,51,52]. Based on this, a preliminary model can be considered for each sample, given the manufacturing settings. Complementary measurements are also advantageous such as the ERDA results in our case. The assumed model is subsequently enhanced using iterative simulations of the reflectivity profiles. Ideally, those iterations—aim to—generate results that agree with the measurements within the experimental uncertainties. The iterative simulations usually resume till meeting the stopping criterion and at that point convergence is assumed. The latter's definition depends on the problem. In our case, the convergence of an inverse-problem is reached when a model enhancement effectively idles and with the results being intelligible. Arguably, such a workflow is the main drawback of reflectometry as a method for determining optical constants. However, we opt for reflectometry because it can determine both parts of simultaneously considering thin films (of any thickness) at any wavelength. The merits of reflectometry in determining optical constants in comparison with other methods are discussed in detail in Ref. [48].

For the relevant inverse-problems here, the dynamical reflectance is calculated using Parratt's formalism combined with Névot–Croce damping factors to account for the effects of interfacial imperfections [53–55]. Sampling the expectation ranges considering the optical and structural characteristics of the assumed models is conducted using Markov chain Monte Carlo (MCMC)-based Bayesian inferences [56–59]. The theoretical background, error modelling, and earlier demonstrations of the aforementioned formalism in determining optical constants are presented in Ref. [48].

Starting with the TiN sample, upon different simulation attempts, the reflectivity data was simulated using two different models. The first model is for the reflectivity data in the range 4.5–8 nm, where two layers on a substrate were assumed, the TiN coating on top of the $SiO_2$ layer on a silicon substrate. The $SiO_2$ layer is the unetched substrate's passivation layer. The second model for the reflectivity data above 8 nm consists

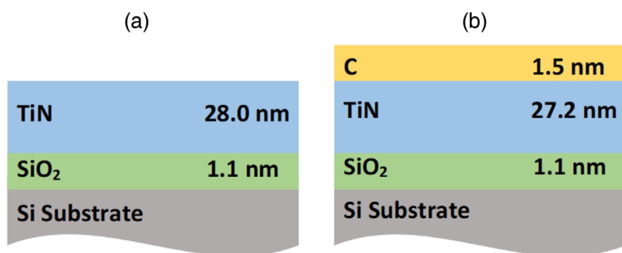


**Fig. 2.** Simulated models of the TiN sample. (a) The model for reflectivity data between 4.5 nm and 8.0 nm. (b) The model for the reflectivity data above 8.0 nm.

of a tri-layer model including a carbon layer. This additional layer estimates the influence of all contamination on the surface, including all physi- and chemi-sorbed species. The presence of contaminates is natural since the sample was handled in the ambience before measurements. For simulations, the calculated thickness of the $SiO_2$ layer in the first model (for data in the range 4.5–8 nm) was fixed for modelling the data above 8 nm. The optical constants of Si and C in the simulations were fixed as taken from CXRO's database [51,52]. The assumed density for the substrates is fixed as the tabulated bulk density of 2.33 $g/cm^3$ [60]. The density of the carbonaceous layer was a free parameter and—seemingly—converged at a density of 1.49 $g/cm^3$. For the $SiO_2$ layer below the TiN coating, its optical constants were taken from Ref. [40], reduced with a factor of 0.8. This factor is needed to account for the decreased density in the natural passivation layer. The models with the thickness indicated upon assuming convergence are shown in Fig. 2.

The use of two different models for the same sample can be explained with the asymmetric sensitivity of reflectivity data to the structural characteristics considering different energies. Another factor could be the influence of possible inaccuracies in the optical data that was fixed for the simulations, especially that no uncertainties are given for those datasets. However, sampling the optical constants of all the constituents in the simulations will lead to an intractable inverse-problem. Such a large number

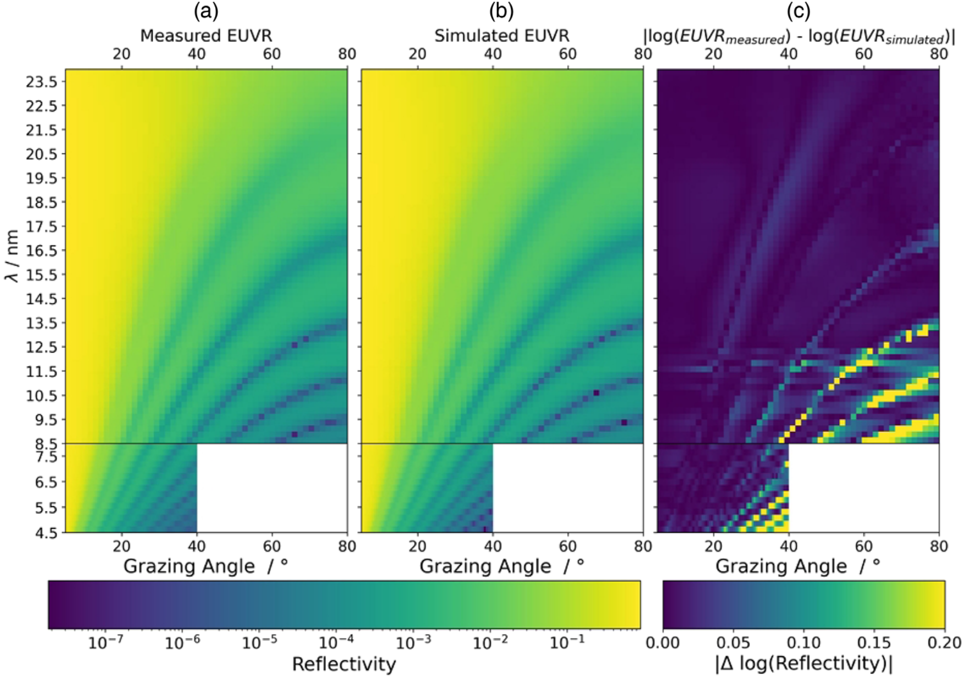


**Fig. 3.** Interpolated representation for measured and simulated reflectivity data of the TiN sample. (a) Measured reflectivity data, (b) simulated data, and (c) mapping of the residual between measurements and simulations.

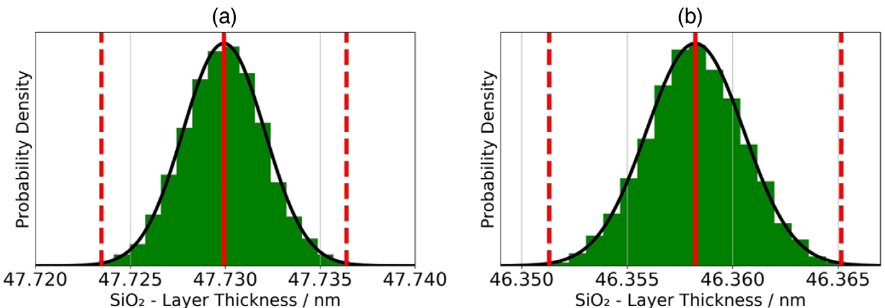


**Fig. 4.** Probability density plots for the calculated thicknesses of $SiO_2$ from the two coupons. The solid and dashed red lines denote the modes of the normal distributions with their 3-$\sigma$ confidence intervals (CIs). (a) Calculated thickness from coupon C-$SiO_2$-A. (b) Calculated thickness from coupon C-$SiO_2$-B.

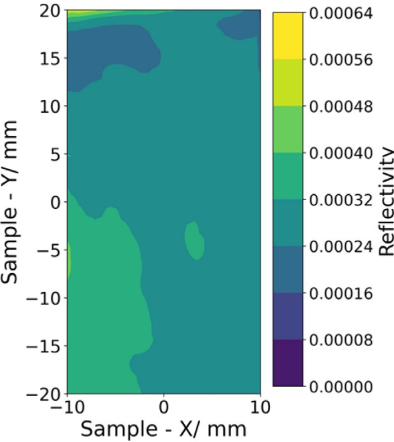


**Fig. 5.** Interpolated mapped reflectance for a part from coupon C-$SiO_2$-A at a wavelength of 13.5 nm and a grazing angle of 65.0° [62].

of free parameters makes the simulations prohibitively time-consuming to attain—the assumed—convergence. Therefore, approximations and assumptions are inevitable to maintain inverse-problems' tractability. Nevertheless, as shown in Fig. 3, the simulated data is in good agreement with the measurements.

We define the residual as the absolute difference between logarithms of the measurements and simulations. The residual between measurements and simulations for the TiN sample peaks in the high grazing angle-high energy range part as shown in Fig. 3(c), specifically, at and in the vicinity of Kiessig fringes' troughs, where the reflectance is lowest. At some intervals, the reflectance in that part is even below $10^{-5}$. Generally, this residual pattern is similar to what was observed in our previous works about determining optical constants from Ru and Ta thin films [48,61].

The plot of the residual in Fig. 3(c) also shows spurts between ca. 11 nm and ca. 12.4 nm. This is due to the non-stoichiometric compounds with non-uniform density profiles forming at the TiN-Si interface, which can be hardly modeled using the discrete-layer approach. It is very difficult to accurately predict the optical constants of such non-stoichiometric compounds in that interface given the anomalous response of Si due to Si-$L_{2,3}$ transitions.

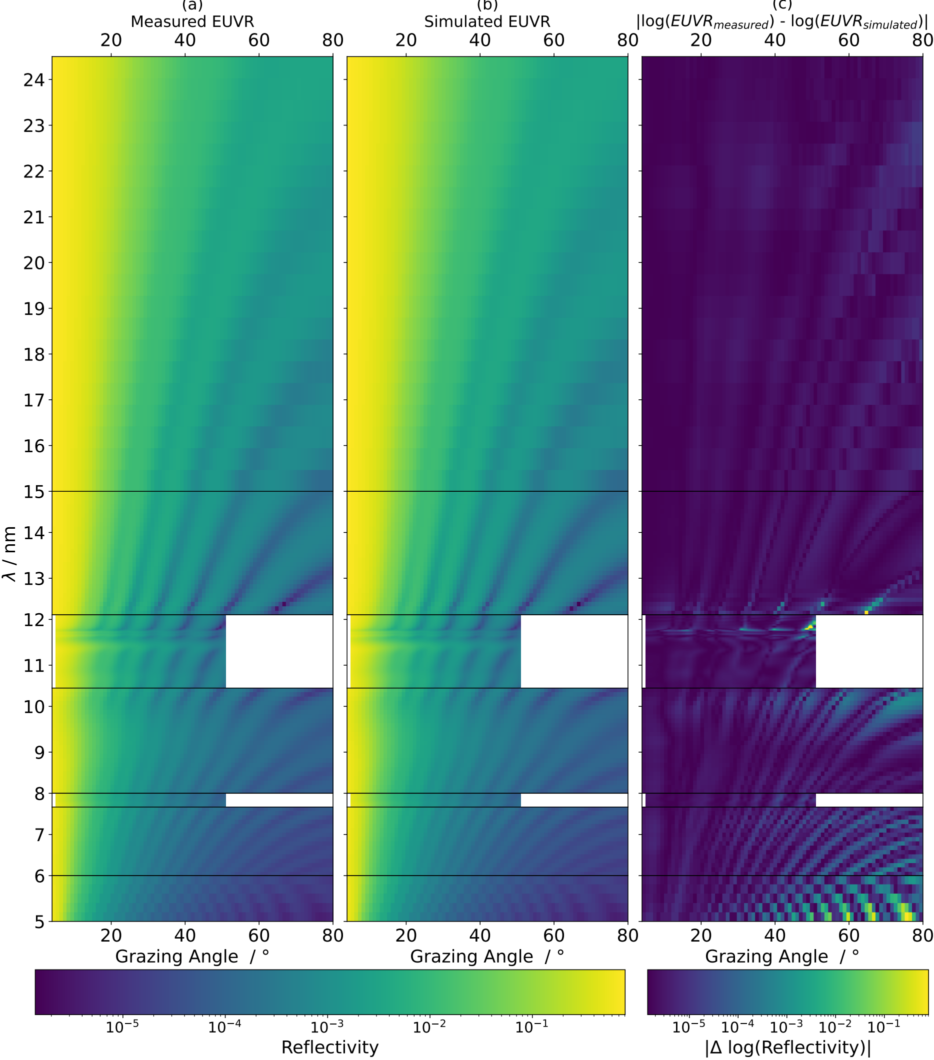


**Fig. 6.** Interpolated representation for measured and simulated reflectivity data of the $SiO_2$ samples. (a) Measured reflectivity data, (b) simulated data, and (c) mapping of the residual between measurements and simulations.

Considering the second compound, for the amorphous $SiO_2$ coating, a single layer on a substrate was assumed for the simulations. The optical constants of $SiO_2$ were fitted, while those of the substrate were fixed from CXRO's database [51,52]. Upon attaining—the assumed—convergence, two different thicknesses were calculated from the two coupons. The modal values are ca. 47.7 nm and ca. 46.35 nm for C-$SiO_2$ -A and C-$SiO_2$ -B, respectively. The values are close to the nominal coating settings of 50 nm and their probability density plots are shown in Fig. 4.

The small deviation between the two calculated thicknesses is expected because of the small nonuniformity of the coating over a full 300-mm wafer. The relatively non-uniform reflectance mapped from part of coupon C-$SiO_2$-A is shown in Fig. 5.

Regarding the $SiO_2$ samples, although a single-layer on a substrate model was used to simulate the reflectivity profiles, a very good agreement is observed between the measurements and the simulations as shown in Fig. 6.

For the SiN sample, a tri-layer on a substrate model was assumed for the inverse-problem. Descendingly, the model consists of a C contamination layer followed by the SiN coating followed by the substrate's passivation layer ($SiO_2$), all on a Si substrate. The stratification is sketched in Fig. 7. In addition to the environmental contamination expected on the surface, F was detected. That could be due to residuals from $NF_3$ gas used to clean and condition the PECVD system. The C layer is assumed to estimate the effect of all contamination species on the surface. The optical constants of C and Si were also fixed from the CXRO database [51,52]. The mass density of the C layer was assumed 1.2 g/ $cm^3$. The optical constants of the assumed $SiO_2$ layer were those determined in our work.

This sample's reflectance was the most difficult to measure properly and subsequently analyze. The fine-structure is more intricate than for $SiO_2$. The other challenge, the sample's reflectance, proved to be highly non-uniform and degrading. Figure 8 shows the degradation of reflectance from an irradiated spot from the sample, in comparison with two less irradiated positions. The black curve in Fig. 8 shows damping in the reflectance from the first irradiated position of the sample. This can be attributed to morphological changes, to rapid growth of contaminates, or to radiation-induced oxidation. Sun *et al*. reported that ultraviolet (UV) radiation—coupled with heating at 400°C—can be used for dehydrogenating amorphous silicon nitride thin films [63]. The EUV irradiation of our sample is not coupled with annealing, but dehydrogenation might have occurred due to the relatively energetic photons. This could be a potential for a morphological change. For the possibilities of contaminate growth and radiation-induced oxidation, they have been investigated before and proven to be serious issues [64–66]. The comparison for the reflectance shown in Fig. 8 was carried out upon observing distorted dispersion profiles, which were calculated from data collected at wavelengths longer than 25 nm from the first irradiated spot. That data is not presented here, although it was incorporated for simulating the structural model. For conciseness, only the reflectivity data from which the optical constants were determined are presented here.

Due to this unpredicted response of the sample, for analyzing reflectivity data collected at different spectral ranges, different models were simulated. More details are given in Table 3. The number and order of the layers were the same in all models, but the calculated thicknesses and interfacial imperfection coefficients were different. In total, four different models were used to simulate the reflectivity data shown in Fig. 9. Three models were used for the data collected below 26.0 nm and a fourth model for the data collected above 26.0 nm.

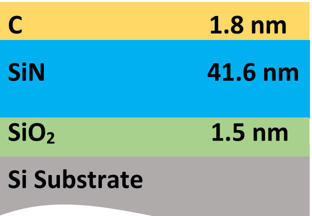


**Fig. 7.** Sketch for the simulated model for the reflectivity data collected in the spectral ranges 5.0–7.0 nm, 8.2–11.0 nm, and 12.4–25.0 nm.

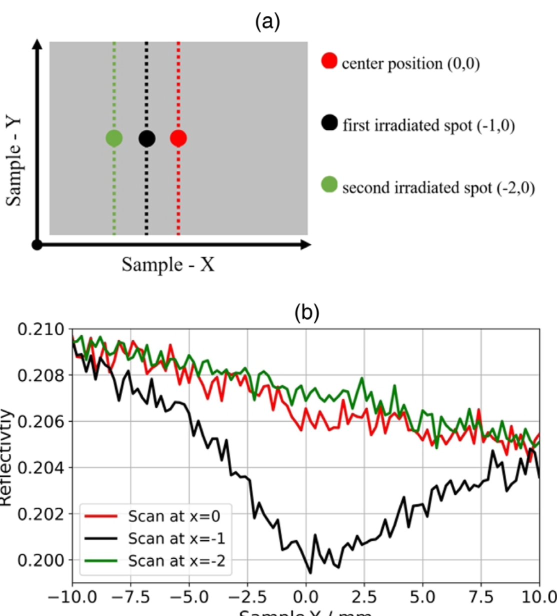


**Fig. 8.** Proof of reflectance degradation of SiN due to irradiation. (a) Sketch of part of the sample with three positions indicated. The dashed lines mark where the scans in (b) were collected. (b) Three reflectivity scans collected at wavelength 13.5 nm and grazing angle 12° from the marked dashes lines in (a).

For Fig. 8 and Table 3, the reflectivity data presented here in the spectral range 26.0–33.0 nm was measured from the green marked spot, while the remaining data was measured from the black marked spot. The second—green marked—spot was irradiated because the determination of optical constants was not possible from reflectivity data measured above 26.0 nm from the first—black marked—spot. Arguably, due to relatively small penetration depths, reflectivity data collected at such long wavelengths is highly affected when characterizing irradiation-damaged spots. Because of the anticipated smaller penetration depths, the thicknesses of $SiO_2$ and SiN were fixed in modelling the data measured in the spectral range 26.0–33.0 nm.

Nevertheless, the simulated reflectivity for SiN is in very good agreement with the measurements as shown in Figs. 9 and 10.

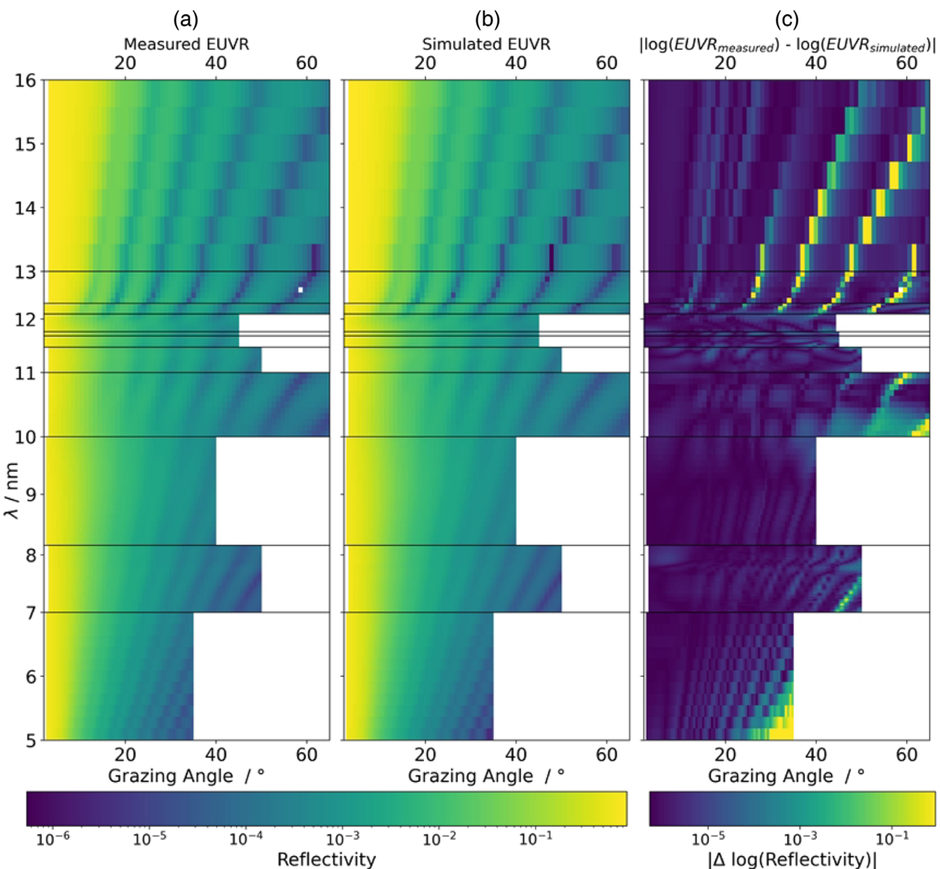


**Fig. 9.** Interpolated representation for measured and simulated reflectivity data of the SiN samples in the spectral range 5–16 nm. (a) Measured reflectivity data, (b) simulated data, and (c) mapping of the residual between measurements and simulations.

**Table 3. Calculated Thicknesses of the Assumed Layers in Modeling the SiN Sample[a]**

| | | Simulated *(and used)* Thicknesses/nm | | |
|---|---|---|---|---|
| **Presented λ-Ranges/nm** | **Irradiated Position** | **C** | **SiN** | **$SiO_2$** |
| 5.0–7.0, 8.2–11.0 and 12.4–25.0 | First | 1.8 | 41.6 | 1.5 |
| ca. 11.53–ca. 12.27 | First | 2.8 | 41.3 | 1.0 |
| 7.1–8.15 and 11.1–11.5 | First | 2.4 | 41.9 | 0.98 |
| 26.0–33.0 | Second | 1.9 | *Fixed* 41.9 | *Fixed* 0.98 |

[a]The simulated thicknesses here relate to additional reflectivity data not presented in this work.

As expected, the residual between measurements and simulations is also highest here at and in the vicinity of Kiessig fringes' troughs. The discussion on the residual of TiN reflectivity maps [Fig. 3(c)] also applies here.

## 4. DETERMINED OPTICAL CONSTANTS

Beginning with TiN, the calculated optical constants depict relatively smooth and increasing functions for the investigated spectral range between 4.5–24 nm, as shown in Fig. 11. Generally, our calculated optical constants are in good agreement with CXRO IAA-based estimations [44,51]. The used atomic scattering factors (ASFs) for Ti to enable IAA-based estimations here are those updated from 2004 [67], not the original tabulations of 1993 [44]. The nominal stoichiometry of TiN (1:1) with mass density of 4.7 $g/cm^3$ was used for calculating the optical constants.

The trends of the calculated TiN dispersion profiles were as expected. Comisso *et al*. determined the optical constants of $TiO_2$ in the spectral range ca. 2.03–48.6 nm [68], and in the spectral range we investigated their data shows similar trends. Both TiN and $TiO_2$ in the spectral range 4.5–24 nm are dominated primarily by the optical response of Ti, given the higher mass and electron densities. The—generally—good agreement between our data and CXRO IAA-based estimations supports our approach in estimating the measured ERDA stoichiometry. However, a thorough comparison requires the mass density of our coatings to be accurately determined in addition to the uncertainties of external literature, but neither is known. A more detailed comparison specifically at a wavelength of 13.5 nm is shown in Fig. 12.

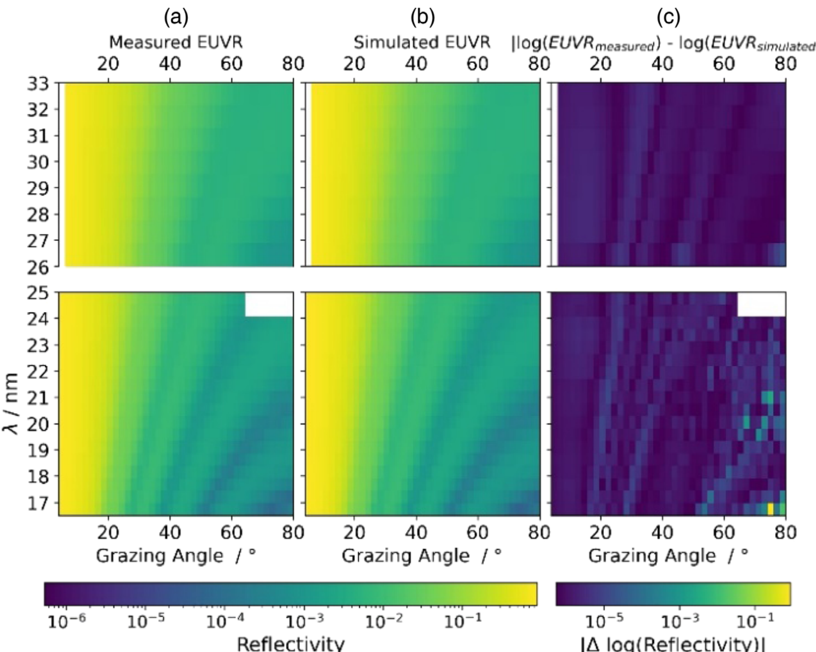


**Fig. 10.** Interpolated representation for measured and simulated reflectivity data of the SiN samples in the spectral range 16.5–33 nm. (a) Measured reflectivity data, (b) simulated data, and (c) mapping of the residual between measurements and simulations.

For the calculated optical constants from the amorphous $SiO_2$ samples, as expected, they reveal a fine-structure around the tabulated atomic transition energies [49]. Our calculated optical constants are plotted in comparison with other literature data in Fig. 13, from Refs. [39–42, 44,51,52,69]. The fine-structures due to the Si-$L_{2,3}$ and Si-$L_1$ transitions are shown in Fig. 14 and Fig. 15, respectively. The theoretical interpretation of Si-$L_{2,3}$ fine-structure in $SiO_2$ is available elsewhere [70–73].

In Figs. 13–15, the two plotted curves referenced Andrle *et al.* refer to two examined crystallographic orientations of a quartz crystal [40], with Miller indices given between parentheses. In most of the investigated spectral range, the dispersion profiles calculated from the quartz crystal [40] are higher than ours.

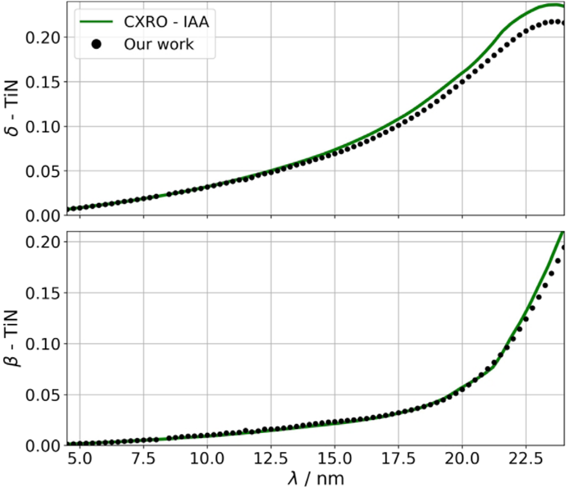


**Fig. 11.** Our calculated optical constants for TiN in comparison with CXRO IAA-based estimations using a mass density of 4.7 g/cm$^3$ between 4.5 and 24 nm [44,51]. Top: profiles of the refractive component. Bottom: profiles of the extinction coefficients.

That can be explained with the higher mass density expected in a bulk crystal in comparison with a thin film.

In Figs. 13–15, Palik data is actually tabulations from two different sources, referenced there in Ref. [39]. Palik data [39] is undersampled around the resolved fine-structure; therefore, no detailed comparison can be conducted. However, it is in general agreement with our results.

In Fig. 13, the data from Ding *et al.* [69] is not shown for the refractive components because it is quite far from all the plotted data there. The optical constants of Ding *et al.* [69] are determined using electron energy loss spectroscopy (EELS), and their EUV data has shown significant inconsistencies regarding other materials before. However, as indicated in Figs. 14 and 15, the noticeable inconsistency between our data and CXRO's [44,51] around Si absorption edges is due to chemical shifts in absorption edges' energies due to oxidation. It is known that such chemical effects are not included using IAA-based estimations. This issue was also pointed out in the PTB's report on determining the optical constants of quartz in the EUV [40].

Another dataset we compare our results with is that of Filatova *et al.* [41]. Filatova *et al.* studied amorphous $SiO_2$ optical constants in the spectral range ca. 0.41 nm–ca 19.0 nm [41]. Above ca. 15 nm, as shown in Fig. 13, there is a clear divergence where our dispersion profiles show a linear increase, while those of Filatova *et al.* [41] trend at a different rate. Also, as shown in Fig. 15, the fine-structures observed in our data and that of Filatova *et al.* [41] are different. This can be attributed to slight differences in the amorphousity of the investigated films. Kurmaev and Wiech measured the emission bands of crystalline and amorphous Si at the $L_{2,3}$ edge and the spectra are clearly different [74]. Crystallinity is generally a factor. H. Philipp showed that amorphous $SiO_2$ reflectance has slightly broadened features in comparison with the crystalline phase, at

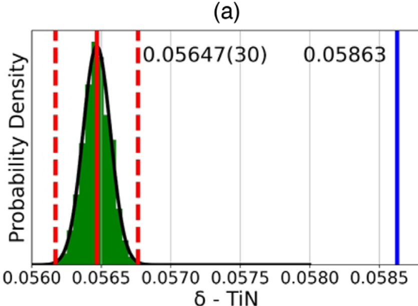

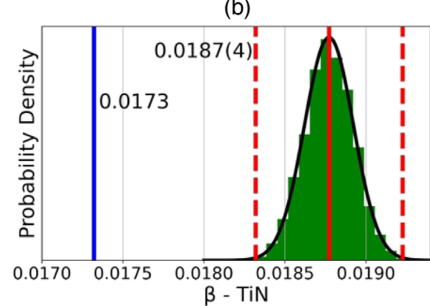


**Fig. 12.** Our calculated optical constants for TiN with their corresponding CIs plotted against CXRO IAA-based estimations (blue lines) at a wavelength of 13.5 nm [44,51]. (a) The refractive component. (b) The extinction coefficient.

energies lower than EUV [75]. Referring to materials other than $SiO_2$, higher crystallinity has been indicated behind "sharper" absorption edges in the EUV range [76,77]. It could be that our sample has lower amorphousity than the one investigated by Filatova *et al*. [41]. Therefore, sharper edges are observed for our sample as clearly shown in Figs. 14 and 15. However, for most of the investigated spectral range here, the extinction coefficients of Filatova *et al*. [41] are smaller than ours, where their refractive indices are higher.

One relevant study to address for discussing inconsistencies between different $SiO_2$ datasets is that of Klinkenberg and Illinsky [78]. They determined optical constants of $SiO_2$ in the spectral range 11.1–13.5 nm from differently prepared thin films; the corresponding results were different [78]. Another factor behind the differences between our optical constants and literature data could be the stoichiometry. Perhaps, there are small variations between the prepared compounds. Barranco *et al*. measured Si K-edge absorption spectra of $SiO_2$, $SiO_{1.7}$, $SiO_{1.3}$, and Si, whose measurement series shows clear differences in the fine-structures of the samples [79].

For the determined optical constants of SiN, they are shown in comparison with external literature in Fig. 16. Figures 17 and 18 show the fine-structures due to Si-$L_1$ and Si-$L_{2,3}$ transitions [49], respectively. As shown in Fig. 16, the IAA-based estimations [44,51,52] assuming the stoichiometry $Si_3N_4$ with mass density of 2.3 g/ $cm^3$ are in general agreement with our results, except for the absorption edges' positions and their fine-structure.

In Figs. 16 and 17, CXRO-Exp refers to the single experimentally determined pair of optical constants using reflectometry at wavelength 13.5 nm for the stoichiometry $Si_3N_4$, as reported in Ref. [38]. Shehzad *et al*. refers to 19 extinction coefficients measured between ca. 13.4 nm and ca 13.67 nm from a membrane with the stoichiometry $SiN_{0.98}$ [37]. In our plots, Windt refers to $Si_3N_4$ optical constants measured at 11.4 nm, 13.55 nm, 17.14 nm, 24.3 nm, and 30.38 nm [80]. The experimental external literature data we found does not properly cover the investigated spectral range to draw a reliable comparison upon. Also, only Shehzad *et al*. provided details about stoichiometry characterization [37]. However, Table 4 lists the values for the experimental optical constants at wavelength 13.5 nm and the numbers are relatively close.

The minor deviation in the extinction coefficients noticed around 25 nm in Fig. 16 is probably due to the addressed

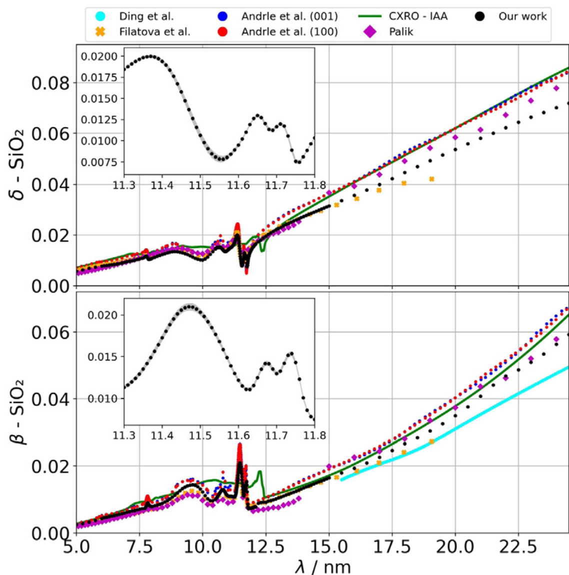


**Fig. 13.** Amorphous $SiO_2$ calculated optical constants in comparison to other literature data in the spectral range 5.0–24.5 nm [39–42,44,51,52,69]. Top: profiles of the refractive component. Bottom: profiles of the extinction coefficients. The sub-plots show parts of the calculated dispersion profiles at the Si-$L_{2,3}$ transitions [49].

sample's damage or expected morphological changes. The determined optical constants above and around 25 nm from the reflectivity data collected from the first irradiated position were different and fluctuating. The optical constants presented here for the spectral range above 25.0 regard our second attempt for reflectivity data from the second irradiated position, with the different positions shown in Fig. 8. It seems this sample is relatively more sensitive to radiation than expected. Therefore, the presented optical constants are vulnerable to additional uncertainties, especially for absorption edges, given indications that the optical constants could vary. However, we present this dataset given the rarity of SiN EUV optical constants.

A final remark: $Si_3N_4$ is known to have two crystal phases, denoted as $\alpha$- and $\beta$-$Si_3N_4$, besides the amorphous, which is the most common [81]. Another polymorph with cubic spinel structure was also reported to form under high temperature and pressure [82]. For synthesizing hexagonal crystalline $Si_3N_4$ samples, Carson and Schnatterly performed crystalline powder pressing [83], while they presented their chemical vapor

**Table 4. Tabulated Experimental Optical Constants of SiN at Wavelength 13.5 nm**

| Source | $\delta$ | $\beta$ | Note |
|---|---|---|---|
| Our work | 0.01929(20) | 0.00626(32) | CIs of 3-$\sigma$ given in concise notation |
| CXRO | 0.021 | 0.0066 | Experimental values from Ref. [38] |
| Shehzad *et al.*[a] | N/A | 0.00652781 | Wavelength very close to 13.5 nm |

[a]From [37].

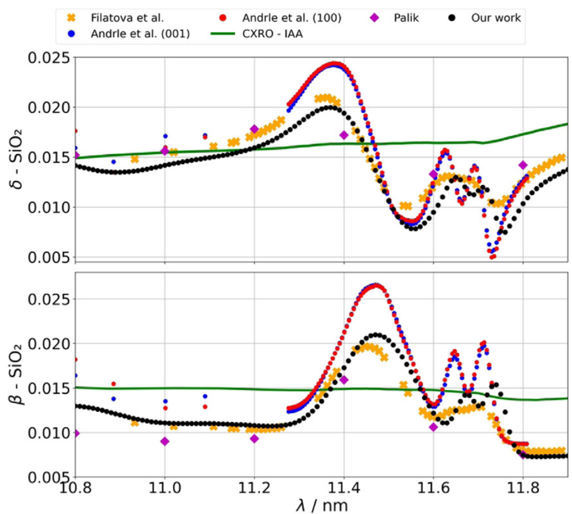


**Fig. 14.** Amorphous $SiO_2$ calculated optical constants in comparison to other literature data in the spectral range 10.8–11.9 nm [39–41,44,51,52].

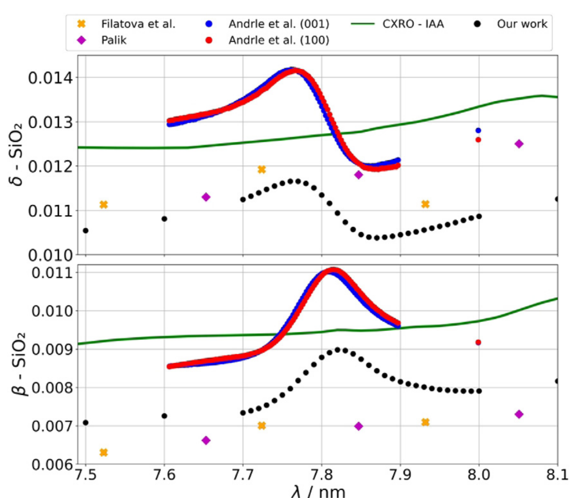


**Fig. 15.** Amorphous $SiO_2$ calculated optical constants in comparison to other literature data in the spectral range 7.5–8.0 nm [39–41,44,51,52].

deposition (CVD) grown film on a Si substrate as amorphous [83]. Here, we also assume our SiN PECVD grown film to be amorphous. However, the film's crystallinity can be critical given that each $Si_3N_4$ phase shows slightly different densities of state (DOS) of the valence-band electrons in the EUV range [83]. Also, stoichiometric differences must also be observed when comparing optical data from different SiN samples. According to Smith *et al*. [84], SiN PECVD grown films are

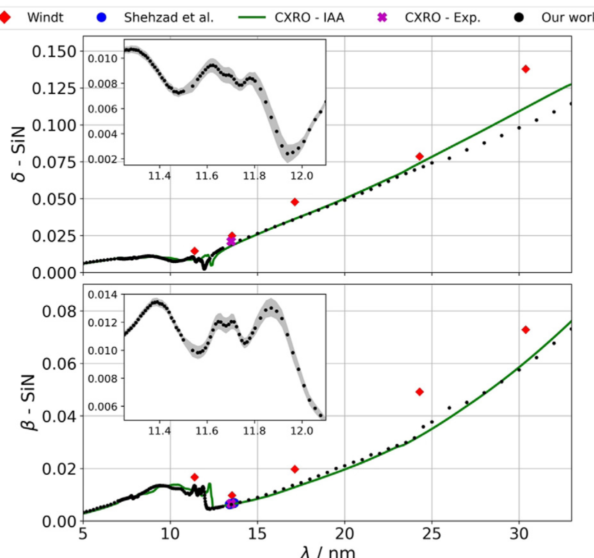


**Fig. 16.** Our SiN calculated optical constants in comparison to literature data in the spectral range 5.0–33.0 nm [37,38,44,51,52,69,80]. Top: profiles of the refractive component. Bottom: profiles of the extinction coefficients. The sub-plots show parts of our dispersion profiles at the Si-$L_{2,3}$ transitions [49]. The gray filled regions in the sub-plots mark the CI of 3$-\sigma$.

generally hydrogenated and non-stoichiometric. Parsons *et al*. discussed reducing hydrogen content in PECVD SiN thin films [85]; the discussion there is relevant for understanding the reasons behind the latter issues. Nithianandam and Schnatterly measured the emission spectra of nearly stoichiometric and non-stoichiometric $Si_3N_4$ thin films in the EUV photon range 65–110 eV; the corresponding spectra are clearly different [86]. Wiech and Šimůnek measured the emission spectra of $\alpha$- and $\beta$-$Si_3N_4$ in the EUV photon range 70–105 eV; the spectra profiles are not identical [87]. In parallel with the discussion following the inconsistencies between the presented $SiO_2$ data, the emphasis on crystallinity and stoichiometry is relevant when attempting to explain inconsistencies between different SiN optical data.

## 5. SUMMARY

We presented the determination of optical constants using synchrotron reflectometry from TiN and amorphous $SiO_2$ thin films in the spectral range 5–24 nm, and from (hydrogenated) SiN in the spectral range 5–33 nm. The measurements and the simulations were shown with emphasis on the used modeling formalism. MCMC-based Bayesian inferences were used to sample the assumed models, which turns over the targeted parameters' uncertainties. We also examined the accuracy of

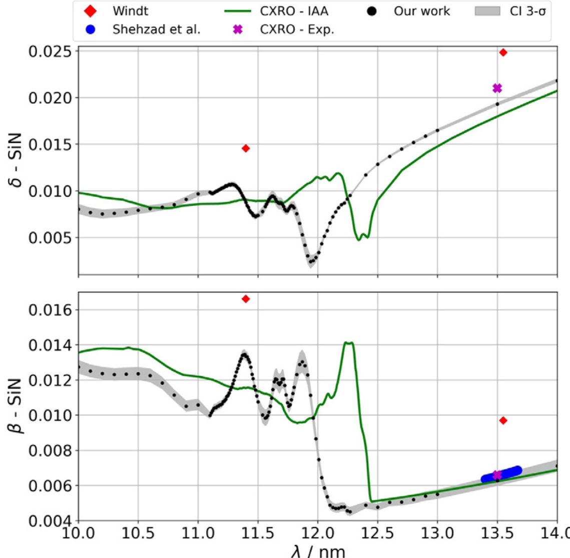


**Fig. 17.** Our SiN calculated optical constants in comparison to literature data in the spectral range 10.0–14.0 nm and at the Si-$L_{2,3}$ transitions [37,38,44,49,51,52,69,80]. Top: profiles of the refractive component. Bottom: profiles of the extinction coefficients. The gray filled regions mark the CI of 3-$\sigma$.

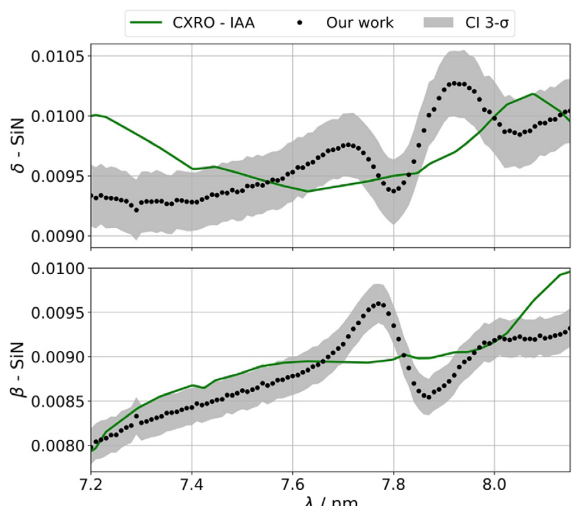


**Fig. 18.** Our calculated SiN optical constants in the spectral range 7.2–8.15 nm in comparison to CXRO predictions assuming the stoichiometry to $Si_3N_4$ [44,51]. The gray filled regions mark the CI of 3-$\sigma$.

the IAA in estimating optical constants in the EUV. The IAA is reliable with limitations considering energy regions coinciding with absorption edges. Additionally, the elemental concentration depth profiles were measured using ERDA, a very sensitive characterization method for light elements providing analyses with high resolution for chemical profiling.

TiN, SiN, and amorphous $SiO_2$ are widely used as constituents of optical elements. The optical constants of both SiN and amorphous $SiO_2$ were adequately sampled to reveal the fine-structure due to the Si-$L_1$ and Si-$L_{2,3}$ transitions. We presented our results with comparisons to external literature. Our results help to improve modeling the optical responses of TiN-, SiN-, and Si-based optical elements and devices dedicated for the EUV range.

The optical constants of TiN, $SiO_2$, and SiN are available on the PTB's online Optical Constants Database (OCDB); [88].

**Funding.** HORIZON EUROPE Framework Programme (20IND04).

**Acknowledgment.** This project has received funding from the EMPIR Metrology for Industry project–Traceable metrology of soft X-ray to IR optical constants and nanofilms for advanced manufacturing (ATMOC). This Joint Undertaking is co-financed by the Participating States and from the European Union's Horizon 2020 research and innovation programme. In our work, measurements were carried out at the Optics Beamline at the BESSY II electron storage ring operated by the Helmholtz-Zentrum Berlin für Materialien und Energie. The authors also thank Analía Fernández Herrero (PTB) for supporting the measurements.

**Disclosures.** The authors declare no conflicts of interest.

**Data availability.** Data underlying the results presented in this paper are not publicly available at this time but may be obtained from the authors upon reasonable request.

## REFERENCES

1. S. Waki, T. Uchida, J. Chen, *et al.*, "High-irradiance illumination system for transmission extreme ultraviolet microscopy," Jpn. J. Appl. Phys. **62**, 050901 (2023).
2. W. Eschen, C. Liu, M. Steinert, *et al.*, "Structured illumination ptychography and at-wavelength characterization with an EUV diffuser at 13.5 nm wavelength," Opt. Express **32**, 3480–3491 (2024).
3. J. Li, K. Li, X. Zhang, *et al.*, "Highly efficient and aberration-free off-plane grating spectrometer and monochromator for EUV—soft X-ray applications," Light Sci. Appl. **13**, 12 (2024).
4. F. Auchère, D. Berghmans, C. Dumesnil, *et al.*, "Beyond the disk: EUV coronagraphic observations of the Extreme Ultraviolet Imager on board Solar Orbiter," A&A **674**, A127 (2023).
5. J. Van Schoot, "The Moore's law machine: The next trick to tinier transistors is high-numerical-aperture EUV lithography," IEEE Spectrum **60**, 44–48 (2023).
6. J. Van Schoot, "Exposure tool development toward advanced EUV lithography: A journey of 40 years driving Moore's law," IEEE Electron Devices Mag. **2**(1), 8–22 (2024).
7. S. Bajt, H. Chapman, N. Nguyen, *et al.*, "Design and performance of capping layers for extreme-ultraviolet multilayer mirrors," Appl. Opt. **42**, 5750–5758 (2003).
8. V. Philipsen, A. Frommhold, D. Thakare, *et al.*, "Mask innovations on the eve of high NA EUV lithography," Jpn. J. Appl. Phys. **63**, 040804 (2024).
9. S. Dutch, "Periodic tables of elemental abundance," J. Chem. Educ. **76**, 356–358 (1999).
10. H.-Y. Chen and F.-H. Lu, "Oxidation behavior of titanium nitride films," J. Vac. Sci. Technol. A **23**, 1006–1009 (2005).
11. D. Gil and D. Windover, "Limitations of x-ray reflectometry in the presence of surface contamination," J. Phys. D **45**, 235301 (2012).
12. D. Petrakov, D. Smirnov, N. Gerasimenko, *et al.*, "Implementation of software for data processing of X-ray optical measurements for the analysis of structural parameters," J. Appl. Cryst. **52**, 186–192 (2019).
13. S. DeVries, E. De Silva, D. Canaperi, *et al.*, "Comparing PVD titanium nitride film properties and their effect on beyond 7 nm EUV patterning," in *31st Annual SEMI Advanced Semiconductor Manufacturing Conference (ASMC)* (2020), pp. 1–5.
14. M. Singh and J. Braat, "Capping layers for extreme-ultraviolet multilayer interference coatings," Opt. Lett. **26**, 259–261 (2001).
15. C. Nicolle, V. Farys, B. Biasse, *et al.*, "A new absorbing stack for EUV masks," Proc. SPIE **5567**, 1417–1424 (2004).
16. J.-H. Yeo, K.-B. Nam, G.-S. Kang, *et al.*, "Development of nanometer-thick graphite film extreme ultraviolet pellicle with hydrogen-resistant TiN capping layer," Mater. Res. Express **9**, 066403 (2022).

17. V. Braic, M. Balaceanu, and M. Braic, "Grazing incidence mirrors for EUV lithography," in *International Semiconductor Conference* (2008), pp. 267–270.
18. A. Kaloyeros, Y. Pan, J. Goff, *et al.*, "Review—silicon nitride and silicon nitride-rich thin film technologies: State-of-the-art processing technologies, properties, and applications," ECS J. Solid State Sci. Tech. **9**, 063006 (2020).
19. R. Mincigrucci, D. Naumenko, L. Foglia, *et al.*, "Optical constants modelling in silicon nitride membrane transiently excited by EUV radiation," Opt. Express **26**, 11877–11888 (2018).
20. V. Tkachenko, V. Lipp, M. Büscher, *et al.*, "Effect of Auger recombination on transient optical properties in XUV and soft X-ray irradiated silicon nitride," Sci. Rep. **11**, 5203 (2021).
21. A. Aminzadeh, M. Bose, D. Smith, *et al.*, "Investigation and optimization of reactive ion etching of $Si_3N_4$ and polyphthalaldehyde for two-step gray scale fabrication of diffractive optics," J. Vac. Sci. Technol. B **37**, 061608 (2019).
22. P. Törmä, J. Kostamo, H. Sipilä, *et al.*, "Performance and properties of ultra-thin silicon nitride X-ray windows," IEEE Trans. Nucl. Sci. **61**, 695–699 (2014).
23. L. Sciortino, M. Barbera, S. Bonura, *et al.*, "Multi-technique investigation of silicon nitride/aluminum membranes as optical blocking filters for high-energy space missions," J. Astron. Telesc. Instrum. Syst. **10**, 018002 (2024).
24. H. Solak, W. Li, D. He, *et al.*, "A new beamline for EUV lithography research," AIP Conf. Proc. **521**, 99–103 (2000).
25. K. Jimenez, P. Nicolosi, L. Juschkin, *et al.*, "Extreme ultraviolet free-standing transmittance filters for high brilliance sources, based on Nb/Zr and Zr/Nb thin films on $Si_3N_4$ membranes: Design, fabrication, optical and structural characterization," Thin Solid Films **695**, 137739 (2020).
26. S. Jin Cho, K. Seo, K. Kim, *et al.*, "Study on the multi layers for EUV pellicle," Proc. SPIE **11517**, 115171E (2020).
27. J. Rothhardt, W. Eschen, C. Liu, *et al.*, "EUV ptychography: material-specific imaging at the nanoscale," Proc. SPIE **12621**, 126210V (2023).
28. S. Bruijn, R. van de Kruijs, A. E. Yakshin, *et al.*, "The effect of Mo crystallinity on diffusion through the Si-on-Mo interface in EUV multilayer systems," Defect Diffus. Forum **283–286**, 657–661 (2009).
29. P. Boher, P. Houdy, L. Hennet, *et al.*, "Silicon/silicon oxide and silicon/silicon nitride multilayers for extreme ultraviolet optical applications," Opt. Eng. **30**, 1049–1060 (1991).
30. H. Xiao, *Introduction to Semiconductor Manufacturing Technology*, 2nd ed. (SPIE, 2012), Sec. 4.2.
31. E. Hasegawa, A. Ishitani, K. Akimoto, *et al.*, "$SiO_2$/Si interface structures and reliability characteristics," J. Electron. Soc. **142**, 273–282 (1995).
32. H.-G. Steinrück, A. Schiener, T. Schindler, *et al.*, "Nanoscale structure of Si/$SiO_2$/organics interfaces," ACS Nano **8**, 12676–12681 (2014).
33. S. Nekrashevich and V. Gritsenko, "Electronic structure of silicon dioxide (a review)," Phys. Solid State **56**, 207–222 (2014).
34. C. Tarrio and S. Schnatterly, "Optical properties of silicon and its oxides," J. Opt. Soc. Am. B **10**, 952–957 (1993).
35. C. Chovino, L. Dieu, E. Johnstone, *et al.*, "EUV mask making: An approach based on the direct patterning of the EUV reflector," Proc. SPIE **5256**, 566–572 (2003).
36. F.-P. Wang, P.-X. Wang, K.-Q. Lu, *et al.*, "Mo/$SiO_2$ multilayers for soft x-ray optical applications," J. Appl. Phys. **85**, 3175–3179 (1999).
37. A. Shehzad, Y. Vesters, D. De Simone, *et al.*, "Photoresist absorption measurement at extreme ultraviolet (EUV) wavelength by thin film transmission method," J. Photonics Sci. Tech. **32**, 57–66 (2019).
38. E. Anderson, W. Chao, E. Gullikson, *et al.*, "Silicon nitride zoneplates and packaging for extreme ultraviolet instruments," J. Vac. Sci. Technol. B **31**, 06F606 (2013).
39. E. Palik, ed., *Handbook of Optical Constants of Solids* (Academic, 1985), Subpart 3.
40. A. Andrle, P. Hönicke, J. Vinson, *et al.*, "The anisotropy in the optical constants of quartz crystals for soft X-rays," J. Appl. Cryst. **54**, 402–408 (2021).
41. E. Filatova, V. Lukyanov, R. Barchewitz, *et al.*, "Optical constants of amorphous $SiO_2$ for photons in the range of 60–3000 eV," J. Phys.: Condens. Matter **11**, 3355–3370 (1999).
42. B. Da, Y. Sun, S. Mao, *et al.*, "A reverse Monte Carlo method for deriving optical constants of solids from reflection electron energy-loss spectroscopy spectra," J. Appl. Phys. **113**, 214303 (2013).
43. E. Filatova, V. Lukyanov, C. Blessing, *et al.*, "Reflection spectra and optical constants of noncrystalline $SiO_2$ in the soft x-ray region," J. Elect. Spect. Rel. Phen. **79**, 63–66 (1996).
44. B. Henke, E. Gullikson, and J. Davis, "X-ray interactions: Photoabsorption, scattering, transmission, and reflection at E=50-30000 eV, Z=1-92," At. Data Nucl. Data Tables **54**, 181–342 (1993).
45. G. Laricchiuta, W. Vandervorst, and J. Meersschaut, "Mass discrimination in elastic recoil detection analysis and its application to $Al_2O_3$ on $MoS_2$," Nucl. Inst. Met. Phys. Res. B **406**(A), 66–77 (2017).
46. F. Scholze, B. Beckhoff, G. Brandt, *et al.*, "High-accuracy EUV metrology of PTB using synchrotron radiation," Proc. SPIE **4344**, 402–413 (2001).
47. M. Richter and G. Ulm, "Metrology with Synchrotron Radiation–a Brief Introduction," PTB-Mitteilungen **124**, 3–6 (2004).
48. Q. Saadeh, "Bayesian inferences and time-frequency analysis assisted determination of optical constants in the extreme ultraviolet range," Ph.D. thesis (Technische Universität Berlin, Inst. für Festkörperphysik, 2023).
49. G. Zschornack, *Handbook of X-ray Data* (Springer, 2007), pp. 195.
50. A. Sokolov, P. Bischoff, F. Eggenstein, *et al.*, "At-wavelength metrology facility for soft X-ray reflection optics," Rev. Sci. Instrum. **87**, 052005 (2016).
51. The updates to the tabulated values of Ref. [44] are accessed using the CXRO online database via this link: https://henke.lbl.gov/optical_constants/asf.html.
52. The periodic table Python package. Compiled by P. Kienzle with contributions from Distributed Data Analysis for Neutron Scattering Experiments (DANSE) project. Accessible via: https://periodictable.readthedocs.io/en/latest/index.html.
53. J. Als-Nielsen and D. McMorrow, *Elements of Modern X-ray Physics*, 2nd ed. (Wiley, 2011), Chap. 3.
54. L. Parratt, "Surface studies of solids by total reflection of X-Rays," Phys. Rev. **95**, 359–369 (1954).
55. L. Névot and P. Croce, "Caractérisation des surfaces par réflexion rasante de rayons X. Application à l'étude du polissage de quelques verres silicates," Rev. Phys. Appl. **15**, 761–779 (1980).
56. D. Foreman-Mackey, D. W. Hogg, D. Lang, *et al.*, "emcee: The MCMC hammer," Publ. Astron. Soc. Pac. **125**, 306–312 (2013).
57. J. Goodman and J. Weare, "Ensemble samplers with affine invariance," CAMCoS **5**, 65–80 (2010).
58. C. Harris, K. Millman, S. van der Walt, *et al.*, "Array programming with NumPy," Nature **585**, 357–362 (2020).
59. S. Lam, A. Pitrou, and S. Seibert, "Numba: a LLVM-based Python JIT compiler," in *Proceedings of the 2nd Workshop on the LLVM Compiler Infrastructure in HPC* (2015), p. 7, pp. 1–6.
60. W. Haynes, ed., *CRC Handbook of Chemistry and Physics*, 95th ed. (CRC Press, 2014), Sect. 4.
61. Q. Saadeh, P. Naujok, M. Wu, *et al.*, "Nested sampling aided determination of tantalum optical constants in the EUV spectral range," Appl. Opt. **61**, 10032–10042 (2022).
62. J. Hunter, "Matplotlib: A 2D graphics environment," Comput. Sci. Eng. **9**, 90–95 (2007).
63. R. Sun, L. Wang, J. Cheng, *et al.*, "Theoretical modeling on hydrogen evolution in ultraviolet light-treated hydrogenated silicon nitride," J. Appl. Phys. **104**, 094103 (2008).
64. K. Boller, R.-P. Haelbich, H. Hogrefe, *et al.*, "Investigation of carbon contamination of mirror surfaces exposed to synchrotron radiation," Nucl. Instrum. Methods **208**, 273–279 (1983).
65. B. Mertens, M. Weiss, H. Meiling, *et al.*, "Progress in EUV optics lifetime expectations," Microelec. Eng. **73–74**, 16–22 (2004).
66. T. Madey, N. Faradzhev, B. Yakshinskiy, *et al.*, "Surface phenomena related to mirror degradation in extreme ultraviolet (EUV) lithography," Appl. Surf. Sci. **253**, 1691–1708 (2006).
67. Y. Uspenskii, J. Seely, N. Popov, *et al.*, "Efficient method for the determination of extreme-ultraviolet optical constants in reactive materials: application to scandium and titanium," J. Opt. Soc. Am. A **21**, 298–305 (2004).

68. A. Comisso, M. Nardello, A. Giglia, *et al.*, “Optical constants of e-beam evaporated titanium dioxide thin films in the 25.5- to 612-eV energy region,” Opt. Eng. **55**, 095102 (2016).
69. University of Science and Technology of China, Ding’s Microsolid Research Group, “Database of Ding’s Microsolid Lab,” accessed on 21-09-2023 via; https://micro.ustc.edu.cn/database/ELF.html.
70. L. Garvie and P. Buseck, “Bonding in silicates: investigation of the Si $L_{2,3}$ edge by parallel electron energy-loss spectroscopy,” Am. Miner. **84**, 946–964 (1999).
71. H. Ma, S. Lin, R. Carpenter, *et al.*, “Theoretical comparison of electron energy-loss and x-ray absorption near-edge fine structure of the Si $L_{2,3}$ edge,” J. Appl. Phys. **68**, 288–290 (1990).
72. P. Aebi, J. Keller, M. Erbudak, *et al.*, “$L_{2,3}$ edge of silicon: theory and experiment,” Phys. Rev. B **38**, 5392 (1988).
73. J. Chaboy, M. Benfatto, and I. Davoli, “Theoretical analysis of x-ray-absorption spectra at the silicon K and $L_{2,3}$ edges of crystalline and amorphous $SiO_2$,” Phys. Rev. B **52**, 10014 (1995).
74. E. Kurmaev and G. Wiech, “X-ray emission spectra and electronic structure of amorphous silicon,” J. Non-Crys. Sol. **70**, 187–198 (1985).
75. H. Philipp, “Optical properties of non-crystalline Si, SiO, $SiO_x$ and $SiO_2$,” J. Phys. Chem. Sol. **32**, 1935–1945 (1971).
76. S. Huber, V. Medvedev, J. Meyer-Ilse, *et al.*, “Exploiting the P $L_{2,3}$ absorption edge for optics: spectroscopic and structural characterization of cubic boron phosphide thin films,” Opt. Mater. Express **6**, 3946–3959 (2016).
77. H.-J. Hagemann, W. Gudat, and C. Kunz, “Photoabsorption coefficient of alloys of Al with transition metals V, Fe, Ni and with Cu and Pr from 30 to 150 eV Photon Energy,” Phys. Stat. Sol. B **74**, 507–521 (1976).
78. E.-D. Klinkenberg and P. Illinsky, “Reflectivity measurements of thin $SiO_2$ layers in the soft-X-ray region,” Cryst. Res. Technol. **23**, 1193–1199 (1988).
79. A. Barranco, F. Yubero, J. Espinós, *et al.*, “Electronic state characterization of $SiO_x$thin films prepared by evaporation,” J. Appl. Phys. **97**, 113714 (2005).
80. D. Windt, “IMD—Software for modeling the optical properties of multilayer films,” Comput. Phys. **12**, 360–370 (1998).
81. Y.-N. Xu and W. Ching, “Electronic structure and optical properties of $\alpha$ and $\beta$ phases of silicon nitride, silicon oxynitride, and with comparison to silicon dioxide,” Phys. Rev. B **51**, 17379 (1995).
82. A. Zerr, G. Miehe, G. Serghiou, *et al.*, “Synthesis of cubic silicon nitride,” Nature **400**, 340–342 (1999).
83. R. Carson and S. Schnatterly, “Valence-band electronic structure of silicon nitride studied with the use of soft-x-ray emission,” Phys. Rev. B **33**, 2432 (1986).
84. D. Smith, A. Alimonda, C.-C. Chen, *et al.*, “Mechanism of $SiN_xH_y$ deposition from $NH_3$-$SiH_4$ plasma,” J. Electrochem. Soc. **137**, 614–623 (1990).
85. G. Parsons, J. Souk, and J. Batey, “Low hydrogen content stoichiometric silicon nitride films deposited by plasma-enhanced chemical vapor deposition,” J. Appl. Phys. **70**, 1553–1560 (1991).
86. V. Nithianandam and S. Schnatterly, “Soft-x-ray emission spectroscopy study of the electronic structure of nonstoichiometric silicon nitride,” Phys. Rev. B **36**, 1159 (1987).
87. G. Wiech and A. Šimůnek, “Analysis of the electronic and local structure of amorphous $SiN_x$:H alloy films in terms of SiK, SiL, and NK x-ray emission bands,” Phys. Rev. B **49**, 5398 (1994).
88. https://www.ocdb.ptb.de/home.

134.30.220.196 {ts '2025-01-24 02:58:15'}